Research Article

Ibrahim Chikowe and Muhammad Dabai Bala*

Cellulosic materials for the removal of ciprofloxacin from aqueous environments

https://doi.org/10.1515/gps-2023-0190
received September 23, 2023; accepted February 20, 2024

Abstract: The feasibility of using cellulose from *Pinus* spp. sawdust from Zomba, Malawi, treated with commercial and lemon-derived citric acid (CA) for ciprofloxacin (CFX) adsorption from water has been tested. Different CA concentrations were used on NaOH-pretreated sawdust for cellulose esterification. The material was analysed using a variety of techniques. Adsorption tests for CFX were performed using the batch method, and the data were analysed using Langmuir, Freundlich, and Temkin's isotherms. The Fourier transform infrared spectroscopy (FTIR) and point of zero charge results showed surface charges increasing (hydroxyl, −OH, and carboxyl, −COOH groups) due to the CA reaction. The Temkin model was the best fit for the experimental data with R^2 test values of 0.9515, while pseudo-second-order was the best fit (R^2 = 0.9999) in an exothermic adsorption process. The adsorption efficiency was 83% on 0.8 g of the material at pH 4 in 20 mL (20 mg·L^{-1}) CFX. The different CA concentrations during sawdust treatment had a negligible impact on morphology. A regression analysis (R^2 and p-values) of structural data showed that the particle size, distance, and crystallinity index had negligible impact, while surface charges and functional groups had a significant impact on adsorption. Overall, the adsorption of CA-treated sawdust material on CFX is satisfactory.

Keywords: pharmaceutical pollutants, ciprofloxacin, citric acid-modified sawdust, Pinus sawdust decontamination

1 Introduction

Adsorption is one of the more effective methods for the transfer, removal, and transformation of active pharmaceutical ingredients (APIs), and various adsorbents have been designed for such applications. The drug delivery applications of adsorbents include pH-sensitive, temperature-sensitive, and porous adsorbents used for the delivery of drugs, such as ultrasonic hydrogels for ciprofloxacin (CFX), oligo-β-aminoesteruratan hydrogen for doxorubicin, and chitosan for paclitaxel [1]. The environmental application includes the removal of pollutants such as drugs and heavy metals from wastewater. Adsorbents have proved superior to conventional water treatment options due to their flexibility in design and operation, low energy consumption, high removal efficiency, nontoxic secondary by-products and sludge, and compatibility with other water treatment systems [2]. Adsorbents such as activated charcoal have also been used to treat chemical overdoses in the stomach [3]. Studies have also tested the potential of using kaolin and bentonite for gut decontamination of fluoroquinolones (CFX hydrochloride, ofloxacin, and norfloxacin) [4]. Adsorbents have also been used in analytical and environmental sciences as solid-phase extraction platforms during sample pre-treatment techniques [5].

The adsorption process interfaces of materials are affected by several factors, such as the presence of water molecules (due to the presence of hydroxyl groups), salts, adsorbent particle size, adsorbate solubility, ionization, pH, and the sample matrices that keep evolving due to industrialization growth and social demands and challenges. These factors have led to limitations among developed adsorbents, which has raised the need for further studies on the widely developed and used adsorbents to have more and improved adsorbents. Biomass-derived materials are promising three-dimensional (3-D) adsorbents due to their large surface area, versatile surface chemistry, easy separation from aqueous media, and easy availability. They are also passive, eco-friendly, renewable, and cost-effective, and there is a growing interest in their research [6,7].

Fluoroquinolones are an important and widely prescribed group of antibiotics [8], and CFX is one of the most prescribed antibiotics in this group. CFX is administered orally, and 15% is metabolized, 45–62% is discharged unchanged in the urine, and 15–25% in faeces. CFX is one of

* **Corresponding author: Muhammad Dabai Bala**, School of Chemistry & Physics, University of KwaZulu-Natal, Westville Campus, Private Bag X54001, Durban 4000, South Africa, e-mail: bala@ukzn.ac.za
Ibrahim Chikowe: School of Chemistry & Physics, University of KwaZulu-Natal, Westville Campus, Private Bag X54001, Durban 4000, South Africa

the drugs that are also widely found in environmental water, such as domestic wastewater and wastewater from hospitals, with as much as 31 mg·L^{-1} being reported from a study in India that worked on effluents of a wastewater treatment plant for pharmaceutical industries [9]. It is also faced with drug overdose in humans [4], and it has delivery challenges to wounds and the stomach [10]. Attempts have already been made to develop adsorbents for antibiotics like CFX from aqueous media, such as wastewater, and these include activated carbon [11], zeolite [12], montmorillonite [13], kaolinite [14], goethite [15], magnetite [16], birnessite [17], and pumice [12]. However, due to the challenges mentioned above, further investigations on adsorbents from biomass are being pursued to produce economical and eco-friendly processes and materials [16,18]. *Pinus* spp. is an abundant biomass with many wastes and by-products, including sawdust. In particular, sawdust is often thrown away but is now commonly utilized as an additive to feedstock and for making useful products related to this work, such as adsorbents and biochar. *Pinus* spp. sawdust is also one of the renewable biomass resources rich in lignin, cellulose, and hemicellulose, which have become sustainable and excellent sources for adsorbent production [18–20]. However, many studies have focussed on the production of biochar rather than the utilization of the raw material through surface and morphological changes. Biochar production involves chemicals and methods that are expensive, high-energy-dependent, and not eco-friendly [18,20]. Furthermore, different sawdust materials from different species have also shown different elemental compositions, such as differences in C, O, H, N, and S atom contents and percent compositions, which may affect their natural and modified physicochemical properties [21]. Citric acid (CA) is naturally occurring, relatively low in toxicity, food-grade, less corrosive, and a cheap acidic chemical modifier [20,22]. Therefore, this study presents a chemically modified low-cost and low-toxicity cellulose adsorbent derived from the sawdust of *Pinus* spp. from Malawi prepared from varying concentrations of CA, a green acid. The adsorbent was utilized for CFX adsorption in aqueous media to remove it as a simulation for wastewater and gut decontamination, drug delivery, and solid-phase extraction.

2 Materials and methods

HPLC-grade CFX, $C_{17}H_{18}FN_3O_3$ (≥98% purity from Sigma Aldrich/Merck), was analysed using a Shimadzu UV-Vis-NIR spectrophotometer UV-3600. The solution pH was measured using a SevenExcellence-Modular Multi-Channel Benchtop pH meter. A DragonLab SK-O330-Pro shaker was used for adsorbate and adsorbent agitation during the batch adsorption method. Boeco filters were used to filter the test materials after adsorption tests. A stainless-steel fine-mesh strainer was used to sieve the sawdust materials. A PerkinElmer Spectrum 100 Fourier transform infrared spectroscopy (FTIR) spectrometer was used to identify the functional groups. Variable particle size sawdust powder was collected from Zomba plateau, Malawi, where *Pinus* spp. (*Pinus patula*, *Pinus orcapa*, *Pinus kesiya*, and *Pinus taeda*) trees are grown and sustainably milled into wooden products. Analytical-grade NaOH, CA, NaCl, and HCl purchased from Merck (SA) were used. All salts and standards for CFX were prepared using deionized water. All analyses were done in duplicate.

2.1 Synthesis of citric acid-treated sawdust cellulose (CATSC)

Meftahi et al. described the reaction between cellulose and CA [23]. Figure S1 shows the pathway for the esterification and partial crosslinking of cellulose in CA solutions.

2.1.1 Step 1 (S1): Sawdust preparation

Sawdust powder was collected and dried thoroughly under a shade at room temperature, sieved using a stainless-steel fine mesh strainer to yield fine-sized (<700 μm) particles, and kept in glass bottles for further studies.

2.1.2 Step 2 (S2): Removal of dust, iron fillings, and water-soluble extractives

A mass of 100 g of fine sawdust powder was added to 2,000 mL of distilled water (pH = 7) and stirred at ~25°C for 1 h using a magnetic stirrer. The supernatant liquid was decanted, and the stirrer was removed (covered with iron fillings). The sawdust was washed repeatedly with deionized water and dried in an oven at 60°C until constant mass (~24 h). About 1 g of the sawdust powder was used for characterization.

2.1.3 Step 3 (S3): Treatment with sodium hydroxide

The S2 sample was taken into a 2,000 mL beaker and mixed with 2,000 mL of 0.025 M NaOH. The mixture was stirred

for 1 h using a magnetic stirrer at ~25°C. The supernatant liquid was decanted, followed by repeated washing with deionized water until it reached a neutral pH. The material was dried in an oven at 60°C until a constant mass (~24 h). About 1 g of the sample was used for characterization.

2.1.4 Step 4 (S4): Treatment with CA

To six beakers (250 mL) containing 5 g of S3 sample each, 50 mL of different concentrations (0.14 M, 0.28 M, 0.42 M, 0.56 M, 1.12 M, and lemon extract) of CA was added. Lemon juice was extracted by cutting, squeezing, filtration, and centrifuging. The S3 sample and CA mixtures were stirred using a magnetic stirrer for 30 min at ~25°C and then heated in an oven at 60°C for 100 min. Excess CA was decanted from the CATSC sample beakers and washed with excess water until neutral. The CATSC was dried in an oven at 60°C until constant mass (48 h). The CATSC was kept in tightly closed glass bottles until analysis. About 1 g of the sample was used for characterization.

2.2 Material characterization

Different characterization methods were used to determine the material morphology, functional groups, and surface charges. The point of zero charge (PZC) (using the salt titration method) was used to identify surface charges. Transmittance FTIR spectroscopy (Perkin Elmer Spectrum 100 FTIR) was used to identify surface functional groups with four scans per minute in the 4,000–400 cm^{-1} range. A scanning electron microscope (SEM) (Zeiss EVO MA 15 EDS/WDS SEM) and a scanning transmission electron microscope (STEM) (using Zeiss Merlin FEG SEM) were used to determine the morphology of the materials. Elemental composition was determined using a Zeiss EVO MA 15 EDS/WDS SEM. An X-ray diffractometer (Rigaku MiniFlex600) was used to determine the crystallinity (crystallinity index and crystallite size) with Cu-Kα radiation at 45 kV and 15 mA from 3 to 90° at a scanning speed of 10° per minute.

2.2.1 PZC determination using the salt titration method

PZC was determined using two salt addition methods, as reported in the literature. The first method was reported by Bakatula et al. [24]. This involved the addition of identical amounts of 40.0 mL of 0.1 M NaCl solution to nine 50 mL beakers containing 200 mg of CATSC substrate. The pH of each beaker was adjusted using 0.1 M HCl and 0.1 M NaOH to 2, 3, 4, 5, 6, 7, 8, 9, and 10 (±0.1 pH units). The initial pH (pH_i) was measured, followed by shaking and measuring the pH (pH_f) again after 24 h of shaking. The two pH values for each beaker were used to calculate the pH change (ΔpH). A pH_f vs ΔpH graph was plotted.

The second method was reported by Al-Maliky [25]. In this method, seven pairs of 50 mL Erlenmeyer flasks containing 20 mL solutions and 1 g each with different pH values were prepared with different amounts of HCl and NaOH solutions (HCl:NaOH:H_2O) ratios: 5:0:15, 4:0:16, 3:0:17, 2:0:18, 0:0:20, 0:3:17, and 0:5:15. The mixtures were shaken for 1 h, followed by an initial pH measurement (pH_i). Then, 1 mL of 0.1 M NaCl was added to each flask and again shaken for 30 min, followed by a final pH (pH_f) measurement. The data were used to calculate the change in pH (ΔpH) to plot a graph of pH_i vs ΔpH. The graph projection's vertical point is the PZC.

2.3 Adsorption studies

2.3.1 CFX preparation

The stock solution was prepared by dissolving the CFX powder in deionized water containing 3 mL of 0.1 M HCl solution. A 100 $mg{\cdot}L^{-1}$ solution was prepared by dissolving 100 mg of pure CFX in a 1 L volumetric flask. The stock solution was diluted to prepare lower concentrations.

2.3.2 Batch adsorption method

The batch adsorption method was used at different adsorbent masses (10–1,000 mg), temperatures (10–65°C), loading doses (0.5–20 $mg{\cdot}L^{-1}$), and pH (2–12 adjusted by the addition of 0.1 M HCl or 0.1 M NaOH dropwise, and contact time of 5–360 min). All experiments, except the mass effect of the parameter studied, were done at 300 mg, 20 mL CFX solution, 25°C, 40 min, 150 rpm, and 20 $mg{\cdot}L^{-1}$ CFX. After analysis, the supernatants were filtered using BOECO filter papers (grade 3 hw, 65 $g{\cdot}m^{-2}$, 125 mm). The CFX concentrations of the control, blank (containing deionized water and 3 mL HCl used in API dissolution), and test materials were analysed using a Shimadzu UV-Vis-NIR spectrophotometer UV-3600 at an average wavelength of 276 nm. Sample concentrations were derived from a calibration curve prepared from different concentrations of CFX.

2.4 Data analysis

The data were assessed for mean ± SD, adsorption or removal efficiency (%), adsorption capacity, and adsorption isotherms [26]. OriginPro 2020b and Microsoft Excel software were used to draw the spectral graphs, tables, and analyses. ImageJ software was used to analyse SEM and STEM images and to calculate particle area, size, and inter-particle distance. Correlations between different influencing parameters were calculated using STATA 17.0 SE – Standard Edition.

CFX adsorption capacity was calculated using the following equation:

$$q_e = \frac{(C_i - C_e)v}{m} \quad (1)$$

where q_e is the adsorbed CFX amount (mg·g^{-1}) at equilibrium time; V is the solution volume (L); m is the adsorbent amount (g); and C_e is the equilibrium CFX concentrations (mg·L^{-1}) at equilibrium time t.

The percent removal or removal efficiency of CFX was calculated using the following equation:

$$R\% = \frac{C_i - C_e}{C_0} \times 100 \quad (2)$$

where C_i is the final CFX concentration and C_0 is the initial concentration at t = 0. Calibration curves were plotted using seven concentrations of standard CFX solutions: 0.5, 1, 5, 10, 15, and 20 mg·L^{-1} and a blank.

Adsorption kinetic data were fitted to the pseudo-first order and pseudo-second order model equations. Adsorption isotherm data were fitted to Freundlich, Langmuir, and Temkin isotherm models. Thermodynamic parameters were calculated at 10°C, 20°C, 30°C, and 45°C with CFX concentrations ranging from 5 to 20 mg·L^{-1}. Gibb's free energy change (ΔG^0), enthalpy change (ΔH^0), and entropy change (ΔS^0) were calculated using standard equations [27]. Adsorption data and the CATSC property correlations were statistically evaluated using regression coefficients (R^2 and p-values).

3 Results

3.1 Material characterization

3.1.1 FTIR spectroscopic analysis

The untreated sawdust cellulose (USC) and CATSC material showed various peak characteristics of the cellulose and sawdust materials. Figure 1 and Table S1 summarize the functional groups identified in the materials.

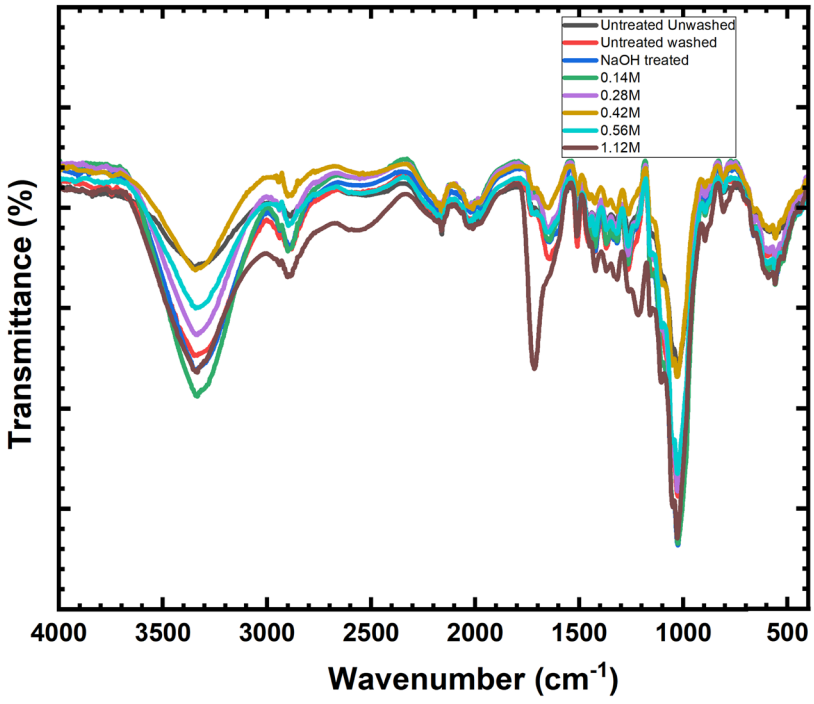

Figure 1: Stacked FTIR absorption spectra of the USC and CATSC materials.

Based on the results, 0.14 and 0.28 M citric-treated cellulose were selected and used as the best adsorbents for the subsequent tests. The lemon-treated material was not used despite having a better removal efficiency compared to the 0.28 M material due to the limited amount of juice needed to produce enough adsorbent for the tests.

3.1.2 PZC

The PZC of 0.14 M CATSC was evaluated and found to be 2.3, indicating that the adsorbent's surface was negatively charged above pH 2.3 and positively charged below it. Figure 2 shows the results of the two PZC tests.

3.1.3 XRD characterization

The XRD characterization data shown in Figure 3 were used to compare crystallinity using the crystallinity index and crystallite sizes of the materials treated with different CA concentrations.

The data shown in Figure 3 were used to calculate the crystallinity index using the peak height method, which is known to undervalue the CI but is good enough for comparative analysis [28]. The crystallite size was also calculated from the data using the Scherrer equation. Table 1 shows the calculated CI and crystallite sizes.

The results show that the CI and crystallite sizes differ for the CATSC with concentration changes, although the differences did not follow any pattern (Table 1).

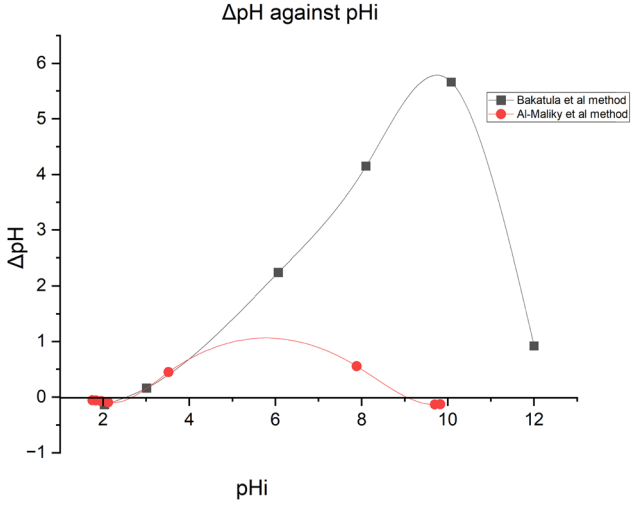

Figure 2: PZC determination for 0.14 M CATSC by the methods of Bakatula et al. (black) [24] and Al-Maliky et al. (red) [25].

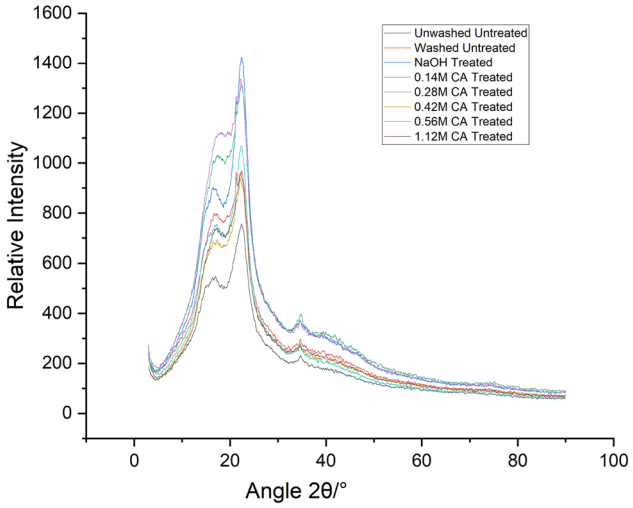

Figure 3: XRD peaks showing the intensities for various CATSC materials.

Table 1: Crystallinity index and crystallite sizes of the USC and CATSC materials

Material	Crystallinity index (CI)	Crystallite size (nm)
Unwashed, untreated	32.24	2.73
Washed untreated	20.69	N/A*
NaOH-treated	41.76	2.00
0.14 M	23.90	1.93
0.28 M	16.26	2.52
0.42 M	28.28	N/A*
0.56 M	33.64	2.16
1.12 M	25.64	N/A*

*N/A: not calculated due to lack of data from the instrument measurements. Manually generated ones would not provide a good comparative analysis with the automatically generated ones.

3.1.4 SEM and STEM analysis

3.1.4.1 Material elemental composition

The changes in the elemental composition of the materials along the treatment line were monitored using SEM EDX, from which the amounts and distribution of the elements were calculated. Significant changes in the C and O atom concentrations were observed in the 0.14 M CATSC material compared to the other materials treated with different acid concentrations. Figure 4 (left) shows how the distribution was measured for one of the materials (0.14 M CATSC). Figure 4 (centre) shows the morphological changes, particularly the surface changes in terms of the pores and breakage of the cellulose, lignin, and hemicellulose structures, that occurred after the treatment with different

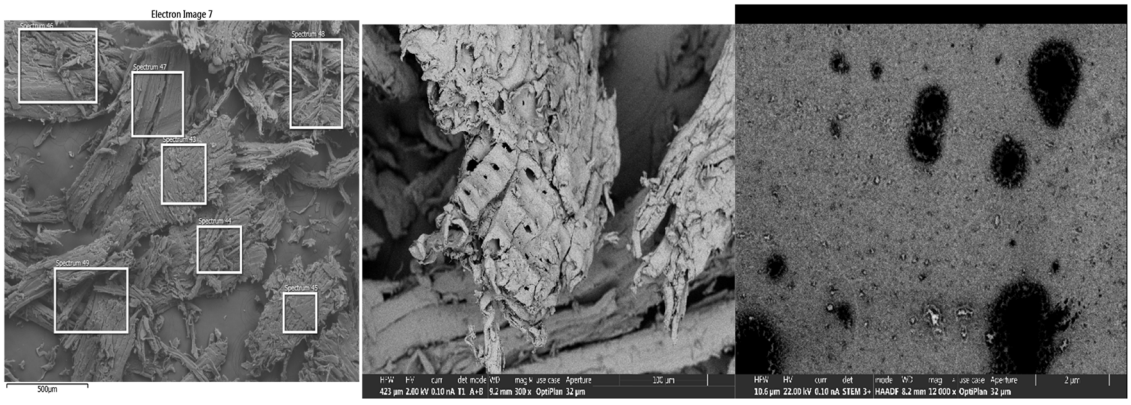

Figure 4: Selected images of the CATSC (0.14 M) material (left: EDX; middle: 300× SEM and right: 12,000× STEM).

Table 2: Elemental composition of USC and CATSC materials

Material	Carbon (C) content	Oxygen (O) content	C/O ratio	Standard deviation	
				Carbon content	Oxygen content
Unwashed, untreated	56.76	43.23	1.31	4.20	4.19
Washed, untreated	54.74	50.97	1.07	2.06	2.04
NaOH-treated	54.09	45.78	1.18	0.32	0.38
0.14 M	66.96	33.04	2.03	0.97	0.97
0.28 M	54.60	45.39	1.19	0.75	0.77
0.42 M	53.94	46.00	1.17	0.61	0.63
0.56 M	54.82	45.17	1.21	0.96	0.97
1.12 M	52.72	47.23	1.12	1.46	1.50

concentrations of CA. Figure 4 (right) shows the irregularly shaped particles and the distribution and sizes of the amorphous (dark) and crystalline (light) areas.

Table 2 compares the elemental composition changes found for all the material phases and their distributions.

The larger elemental standard deviation showed huge elemental distribution variations across the material surfaces, which meant a non-uniform material structure.

3.1.4.2 Particle analysis

The STEM images (Figure 4) were analysed for amorphous and crystalline particles' average distances and areas or sizes. Tables 3 and 4 summarize the results.

3.2 Adsorption of CFX on USC and CATSC materials

The USC and CATSC materials from different CA concentrations were comparatively tested for CFX adsorption. Figure 5 summarizes the adsorption results for the USC and CATSC materials.

Table 3: Particle area and particle distances of the amorphous particles in the untreated and CATSC materials based on STEM image data

Material	Amorphous							
	Particle area/size (µm^2)				Particle distance (µm)			
	Mean	Min	Max	SD	Mean	Min	Max	SD
Untreated, unwashed	0.027	0.0008	1.451	0.102	2.118	0.331	6.128	1.261
Untreated, washed	0.01	0.0008	11.443	0.158	6.115	0.797	18.485	3.552
NaOH-treated	0.167	0.0008	13.794	0.608	2.196	0.499	5.946	1.251
0.14 M	0.004	0.0004	9.686	0.09	0.507	0.037	2.074	0.408
0.28 M	0.002	0.0004	28.485	0.1	0.085	0.027	0.334	0.05
0.42 M	0.094	0.0008	1.718	0.21	3.203	0.644	10.704	2.211
0.56 M	0.006	0.0008	4.502	0.095	0.921	0.048	12.069	1.717
1.12 M	0.002	0.0004	87.806	0.238	0.087	0.024	0.306	0.066

Table 4: Particle area and particle distances of the crystallite particles in the untreated and CATSC materials based on STEM image data

Material	Crystalline							
	Particle area (μm^2)				Particle distance (μm)			
	Mean	Min	Max	SD	Mean	Min	Max	SD
Untreated,unwashed	0.001	0.0008	0.256	0.011	3.521	0.553	10.614	1.993
Untreated, washed	0.0009	0.0007	0.643	0.007	0.295	0.049	1.828	0.31
NaOH-treated	0.001	0.0008	0.253	0.005	0.728	0.083	2.384	0.484
0.14 M	0.0009	0.0004	1.314	0.005	0.073	0.024	0.209	0.04
0.28 M	0.001	0.0004	0.612	0.005	0.076	0.024	0.512	0.083
0.42 M	0.0009	0.0008	1.189	0.01	0.498	0.037	4.414	0.547
0.56 M	0.001	0.0008	0.368	0.006	0.205	0.042	0.979	0.178
1.12 M	0.0006	0.0004	0.706	0.005	0.22	0.023	0.778	0.188

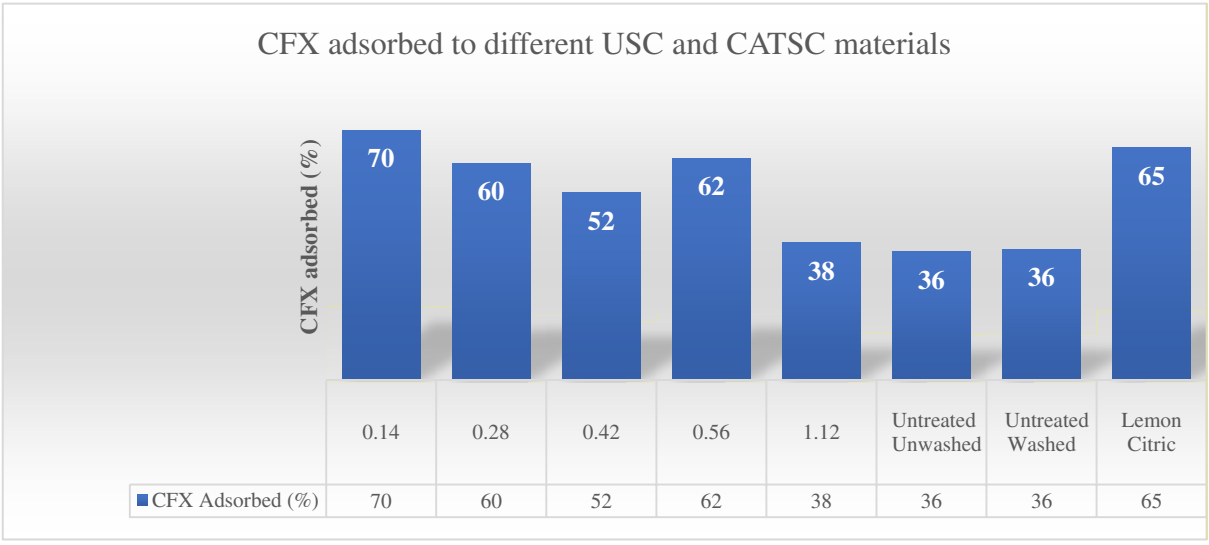

Figure 5: CFX removal efficiencies of the various cellulosic materials.

The results presented in Figure 5 show that at pH 4 with 20 mL of 20 mg·L^{-1} using 0.3 g of the adsorbate, CATSC treated with 0.14 M had the highest CFX removal efficiency of 74%, followed by lemon CA (65%), 0.56 M CA (62%), 0.28 M CA (61%), 0.42 M CA (53%), 1.12 M CA (39%), untreated washed cellulose (36%), and untreated unwashed cellulose (36%).

However, the activity showed an irregular removal efficiency trend among the CATSC materials as the CA concentration increased, as shown in Figures 5 and 6.

3.3 Factors that affected the removal efficiency and capacity of the best-performing materials

Various factors were evaluated to find out how they would affect the CFX adsorption efficiency of the 0.14 and 0.28 M CATSC materials, and the assessed parameters were the reaction time, mass of adsorbent used, pH of the reaction solution, loading dose of CFX, and temperature.

3.3.1 Effect of a loading dose or initial concentration on the removal efficiency of CFX

Different loading doses of CFX were tested to determine their effects on removal efficiency. The results showed that the increase in loading dose decreased the removal efficiency. Figure 7a shows a summary of the results.

3.3.2 Effect of adsorbent dose on the removal efficiency of CFX

The increase in the adsorbent dose also increased CFX removal efficiency. Figure 7b shows the graph of removal efficiency as the adsorbent dose increased.

Table 5: Isotherm data for 0.14 M CATSC adsorption on the CFX

Models	Constants	Value
Highest efficiency	%	83
Highest adsorption capacity	$mg{\cdot}L^{-1}$	2.04
Freundlich	Equation	$\ln q_e = \ln k_f + \frac{1}{n}\ln C_e$
	R^2	0.7868
	n_f	0.6173
	K_f	0.3566
Langmuir	Equation	$\frac{I}{q_e} = \frac{1}{k_L q_m}\left(\frac{1}{C_e}\right) + \frac{1}{q_m}$
	R^2	0.6721
	Q_m ($mg{\cdot}g^{-1}$)	−0.5395
	k_L	−0.1435
	R_L	1.0773
Temkin	Equation	$q_e = B_T{\cdot}\ln AT + B_T{\cdot}\ln C_e$
	R^2	0.9515
	B	0.8570
	K_T	0.7051
Thermodynamic parameters	Equation	$\Delta G^0 = -RT \ln K_c$
	ΔH	−6.0184
	ΔS	−33.3724
	ΔG (10°C)	3.4853
	(25°C)	3.851
	(35°C)	4.1761
	(45°C)	4.695
Pseudo-first-order	Equation	$\ln(q_e - q_t) = \ln q_e - k_1 t$
	R^2	0.7296
	K_1	−0.0024
	q_e	0.3998
Pseudo-second-order	Equation	$\frac{t}{q_e} = \frac{1}{k_2 q_e^2} + \frac{1}{q_e}$
	R^2	0.9999
	K_2	1.03
	q_e	1.0398
Intraparticle diffusion	Equation	$q_t = \text{Cid} + K_{id}t^{½}$
	R^2	1, 1, 0.9768, 1
Chemisorption	Equation	$\frac{t^{\frac{1}{2}}}{q_t} = t^{\frac{1}{2}}\left(\frac{1}{q_e}\right) + \frac{1}{K_{dc}}$
	R^2	0.9981
	q_e	0.9158

3.3.3 Effect of solution pH on the removal efficiency of CFX

The pH of a solution plays a significant role in the adsorption processes because it determines the adsorbent surface charges and, hence, the nature of interactions between the adsorbate and adsorbent [29]. A series of experiments were performed using 20 $mg{\cdot}L^{-1}$ CFX solutions at different pH values (i.e., pH 2–12) to investigate the effect of pH on removal efficiency, and the results are shown in Figure 7c.

Figure 7c shows that the percentage removal of CFX increased with the increasing solution pH until the maximum removal occurred in the pH range of 4.5–5. The removal efficiency decreased slightly to pH 6, after which the efficiency increased slowly. The removal efficiency behaviour was attributed to the adsorbents' surface charge and the CFX state across the different pH ranges. The substrate's performance depends on many factors, such as surface functional groups, the presence or absence of anions and cations, the availability and size of the porous structure in the precursors [30] and the PZC, or isoelectric point, a pH value at which the surface charge components become equal to 0 (equal amounts of positive and negative charges). The differences in the performance of the material at varying reaction pHs are attributed to the chemical changes observed in both the material and the CFX across the pH gradient. This is illustrated in Figure 7d, which highlights the zwitterionic state of CFX (pH 6–9) [24].

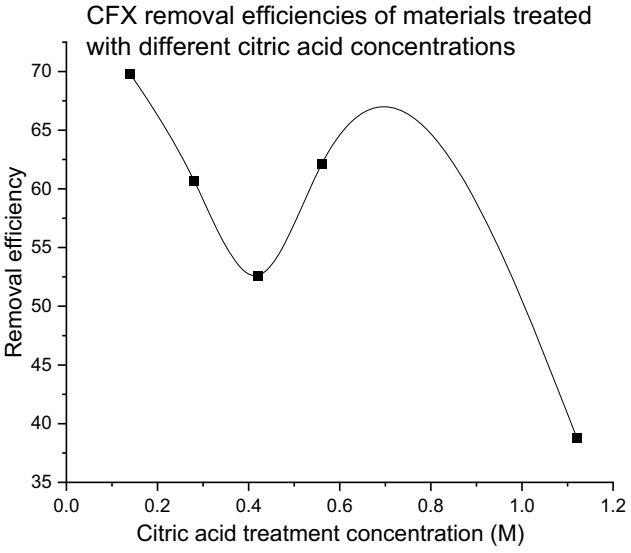

Figure 6: Removal efficiency trends.

The CFX molecules exist in various forms at different pH values. The first dissociation constant (pKa_1) corresponds to the carboxylic acid group, and the second acid dissociation constant (pKa_2) corresponds to N-moiety groups. When the pH is less than pKa_1, the amine group is protonated, and the CFX^+ (cationic) form dominates the solution. When the pH value exceeds pKa_2, the carboxyl and N-moiety groups get deprotonated, giving CFX^- (anionic) form as a dominant species [26].

3.3.4 Effect of contact time on the removal efficiency of CFX

Contact time was also studied to determine its effect on CFX adsorption on the material. Figure 7e shows the trends in removal efficiency with time.

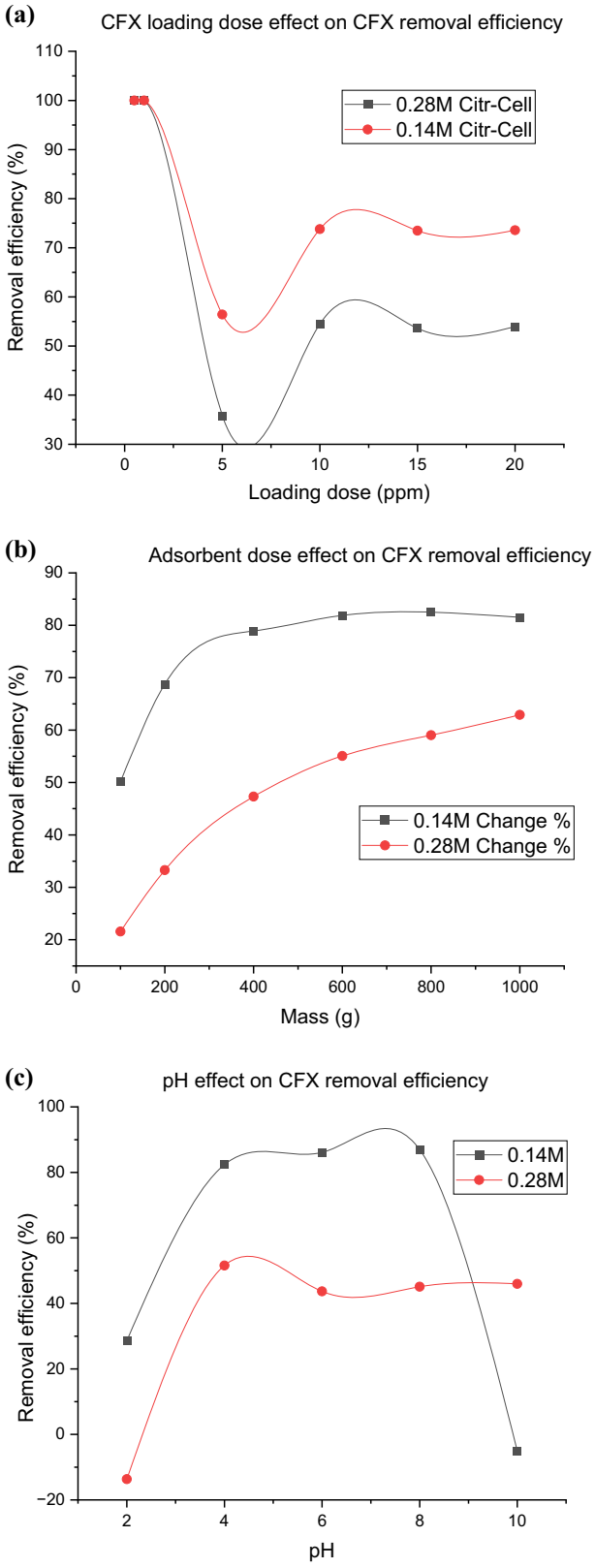

Figure 7: (a) Effect of loading dose on the removal efficiency of CFX. (b) Effect of adsorbent dose on the removal of CFX. (c) Removal efficiency as a factor of pH. (d) States of CFX in different pH solutions and schematic illustration of the mechanism of adsorption for zwitterionic CFX onto CATSC materials via H-bonding, electrostatic attraction, and π–π interactions. (e) Effect of contact time on the removal efficiency of CFX. (f) Effect of temperature on the adsorption of CFX.

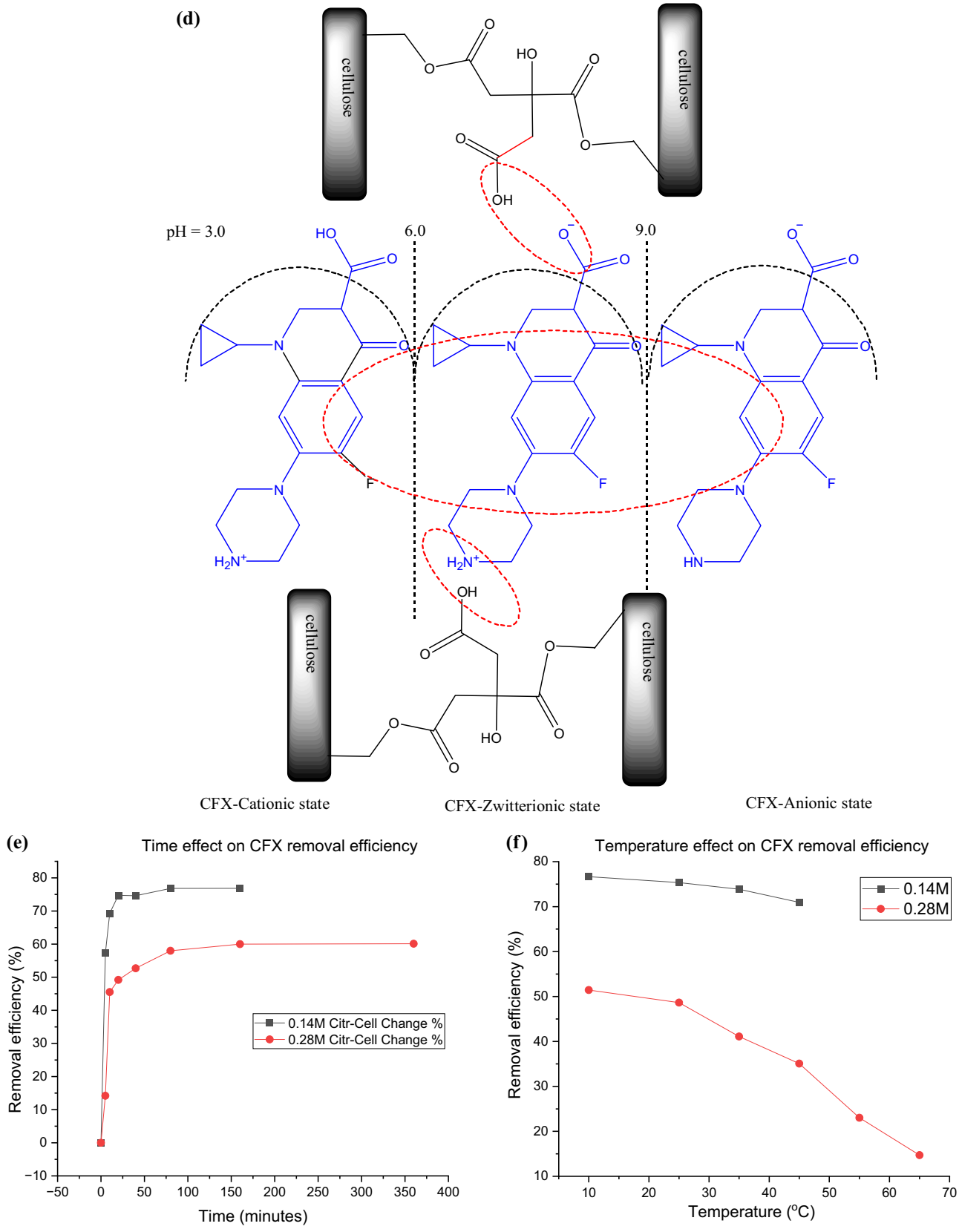

Figure 7: (*Continued*)

Figure 7e shows that removal efficiency increased at a decreasing rate of up to 75% at 40 min when the CFX removal remained almost constant, showing that an equilibrium state had been reached.

3.3.5 Effect of temperature on the removal efficiency of CFX

The temperature effect on the CFX removal efficiency of the material was investigated, and it was found that the temperature increase reduced the removal efficiency of the material. Figure 7f shows a plot representing the phenomenon.

3.4 Adsorption isotherms

Adsorption can occur through various mechanisms, such as cation exchange, surface complexation, cation bridging, and hydrogen bonding. Adsorption processes can be classified mainly into two groups: chemical adsorption and physical adsorption. In physical adsorption, the forces between the adsorbate and solid surface are relatively weak (mostly van der Waals interactions), while the forces in chemical adsorption are strong. In chemical adsorption, the formation of chemical bonds takes place between the adsorbate and the solid surface. In physical adsorption, the nature of the process is reversible. However, in chemical adsorption, detachment of adsorbed compounds from a solid surface can be difficult [19,31,32]. Typically, the adsorption process relies on many steps, i.e. three consecutive steps [33]. The three steps start with an improvisation or external adsorption process, followed by an intraparticle diffusion phase that involves gradual adsorption occurring when intraparticle diffusion is rate-limiting, and lastly, a final equilibrium phase when intraparticle diffusion slows down because of the significant decrease in the adsorbate concentration. Intraparticle diffusion is a rate-limiting step when the regression line passes through the origin. When the regression line does not pass through the origin, other mechanisms, apart from intraparticle diffusion, contribute to the adsorption process [34]. These parameters were investigated to determine if they had an impact on the adsorption process.

Adsorption isotherms were determined by Langmuir, Freundlich, and Temkin's isotherm models, which were applied to the adsorption experimental data to investigate the nature of the interaction between CFX and the materials. The analyses and results of the isotherms are summarized in Table 5 and described below.

3.4.1 Langmuir isotherm model

The Langmuir isotherm model is described by the following linearized expression [35,36]:

$$\frac{I}{q_e} = \frac{1}{k_L q_m}\left(\frac{1}{C_e}\right) + \frac{1}{q_m}$$

where q_e is the adsorption capacity determined at equilibrium ($mg{\cdot}g^{-1}$); q_m is the maximum adsorption capacity ($mg{\cdot}g^{-1}$); and k_L is the Langmuir constant ($L{\cdot}mg^{-1}$). The Langmuir plot constructed between $1/q_e$ and $1/C_e$ yielded a straight-line equation $\frac{1}{q_e} = 12{\cdot}92\left(\frac{1}{c_e}\right) - 1{\cdot}85$ with a correlation coefficient (R^2) = 0.6721 (Figure S2 and Table 5).

The q_m and k_L values were calculated and found to be $-0.5395\ mg{\cdot}g^{-1}$ and $-0.3119\ L{\cdot}mg^{-1}$, respectively. The most characteristic property of the Langmuir isotherm is given by RL (separation factor, a dimensionless quantity), where RL = 0 indicates irreversible isotherm; 0 < RL < 1 indicates favourable isotherm; RL = 1 indicates linear isotherm; and RL > 1 indicates unfavourable isotherm [37]. The RL value (at initial CFX concentration) was calculated to be 1.0773 using the expression $RL = 1/1 + k_L C_i$, where C_i is the initial adsorbent concentration ($mg{\cdot}L^{-1}$). The RL value is greater than 1, and the negative slope in this study indicates that the Langmuir isotherm equation is an unfavourable fit; the material surface is homogenous and gives non-monolayer adsorption of CFX [38].

3.4.2 Freundlich isotherm

The Freundlich isotherm model is described by the linearized expression

$$\ln q_e = \ln k_f + \frac{1}{n}\ln C_e$$

where k_f is the adsorption capacity and n is the intensity of adsorption.

When the Freundlich constant ($1/n$) is between 0 and 1, it means heterogeneous surfaces; if the value of $n > 10$, then the isotherm is irreversible, while $n > 1$ means preferential adsorption and "n" <1 means poor adsorption [39]. The Freundlich plot constructed between $\ln q_e$ and $\ln C_e$ yielded a straight line with a coefficient of correlation of R^2 = 0.7868, as shown in Figure S3 and Table 5.

The k_f and n values were calculated and found to be 0.3566 and 0.6173, respectively. The low value of n (<1) showed that there was poor adsorption potential, while the value of $1/n > 1$ (1.6573) means cooperative adsorption and homogeneity [36].

3.4.3 Temkin isotherm

The Temkin's isotherm model is described by the linearized expression [40]

$$q_e = B_T \ln AT + B_T \ln C_e$$

where B_T (heat of adsorption in J·mol^{-1}) = R_T/b_T; A_T is the equilibrium-binding constant of the isotherm L·g^{-1}; b_T is the Temkin isotherm constant; R is the universal gas constant (8.314 J·mol^{-1}·K^{-1}); and T is the temperature (298 K). Temkin's plot constructed between q_e and ln C_e yielded a straight line with a coefficient of correlation of R^2 = 0.9515, as shown in Figure S4 and Table 5.

The K_T and B_T values were calculated and found to be 0.7051 L·g^{-1} and 0.8570 J·mol^{-1}, respectively. The positive value of BT indicated that the reaction was exothermic. This result agreed with the observation that an increase in temperature led to a decrease in removal efficiency.

The correlation coefficients for Langmuir, Freundlich, and Temkin's isotherm models indicated a weak relationship between the chosen variables, as the R^2 values were less than 0.99. However, the Temkin isotherm model had a higher correlation coefficient (0.9308) than the Freundlich (0.8491) and Langmuir (0.7704) isotherm models. In addition to the R^2 value calculation, a statistical approach (an error function called chi-square) was used to compare the goodness of fit of the adsorption isotherms. The chi-square values for the Langmuir, Freundlich, and Temkin isotherms were 0.8840, 0.9262, and 0.9837, respectively. The highest R^2 and χ^2 values were obtained using Temkin's model, indicating that it best described the uptake of CFX.

3.4.4 Adsorption thermodynamics

The orientation and feasibility of CFX uptake into the material were assessed thermodynamically using Gibb's free energy (ΔG^0) at room temperature using the following equation:

$$\Delta G^0 = -RT \ln K_c$$

where K_c (equilibrium constant) = q_e ×1,000/C_e; R is the universal gas constant (8.314 J·K^{-1}·mol^{-1}); and T is the absolute temperature (K). Figure S5 and Table 5 show the thermodynamic model plot.

ΔG^0 was calculated and found to be 4.695 kJ·mol^{-1}, while ΔH^0 and ΔS^0 were −6.02 and −33.37 kJ·mol$^{-1,}$ respectively. Hence, the positive uptake of CFX onto chemically modified material was non-spontaneous and thermodynamically unfavourable. This meant an increment in temperature (>298 K) would affect the uptake of CFX, which was also observed experimentally when the effect of temperature on adsorption capacity and removal efficiency were investigated. A negative ΔH value suggests that the sorption process was exothermic, as also shown in the temperature effect in this study (temperature). A negative ΔS value suggests decreased randomness at the solid-solution interface during the adsorbate fixation at the adsorbent's active sites. This also meant that solvent molecules occupying the adsorbent surface were not easily displaced by CFX molecules, which might have hindered the adsorption capacity [41].

3.4.5 Adsorption kinetic model

Pseudo-first-order and pseudo-second-order kinetic models were used to study the efficiency of CFX removal.

3.4.5.1 Pseudo-first-order kinetic model

The linearized pseudo-first-order kinetic model is represented by ln ($q_e - q_t$) = ln $q_e - k_1 t$, where q_t is the adsorbate amount in mg on to adsorbent (g) at time t (min) and k_1 is the rate constant (min^{-1}). Ln($q_e - q_t$) was plotted against t and provided a straight correlation of ln($q_e - q_t$) = −0.0969t − 0.9169 with a coefficient of correlation (0.7296), as shown in Figure S6 and Table 5.

The data satisfied the pseudo-first-order requirements for 1 point only; the experimental (1.0333) and calculated (0.3998)q_e values are far from each other. The low R^2 value also indicates that the kinetic model did not fit the experimental data.

3.4.5.2 Pseudo-second-order model

The adsorption data were analysed for a pseudo-second-order kinetic model equation thus:

$$\frac{t}{q_e} = \frac{1}{k_2 q_e^2} + \frac{1}{q_e}$$

where k_2 is the pseudo-second order rate constant (g·mg^{-1}·min^{-1}). A plot of t/q_t against t was obtained (Figure S7 and Table 5), which provided a straight-line equation t/q_t = y = 0.9617t + 0.8980 with a correlation coefficient equal to 0.9999.

The q_e value was calculated from the plot and found to be 1.04 mg·g^{-1}, which is very close to the experimental value of 1.03 mg·g^{-1}. The pseudo-second-order correlation coefficient (R^2 = 0.9999) was very high and close to 1, with all the data points on the line of best fit. Therefore, the data

best fit the pseudo-second-order kinetic model and suggests that the adsorption of CFX is favoured or controlled by the chemisorption process, supporting the multilayer adsorption onto the adsorbent surface. This suggests that the adsorption process involved intermolecular interactions between the material and CFX molecules, particularly close contacts such as π–π interactions and hydrogen bonding [39].

3.4.6 Kinetic adsorption mechanism

The kinetic adsorption mechanism was analysed using the Weber and Morris intraparticle diffusion model and the diffusion–chemisorption model [36].

3.4.6.1 Intraparticle diffusion model

The intraparticle diffusion model was used on the data to investigate the rate-determining step [36]. The equation for the Weber and Morris intraparticle diffusion model is illustrated using the following equation:

$$q_t = \text{Cid} + K_{id}t^{½}$$

where K_{id} is the intraparticle diffusion rate constant ($mg{\cdot}g^{-1}{\cdot}min^{-1/2}$) and Cid is the boundary layer thickness ($mg{\cdot}g^{-1}$), which is a constant parameter. The plot of q_t versus $t^{1/2}$ yielded a multilinear relationship, as shown in Figure S8 and Table 5, which means that the adsorption process involved different phases of the material.

The linear equation provided the intercepts of 0.7869, 0.4038, and 1.0324, which suggests that intraparticle diffusion might have played a significant role in the adsorption of CFX but was not a rate-determining step because the regression line did not pass through the origin (0) [42]. However, the lower R^2 value suggests otherwise.

3.4.6.2 Diffusion–chemisorption model

The diffusion–chemisorption model was selected to describe the adsorption of CFX onto the CATSC. The equation is expressed as follows:

$$\frac{t^{\frac{1}{2}}}{q_t} = t^{\frac{1}{2}}\left(\frac{1}{q_e}\right) + \frac{1}{K_{dc}}$$

where K_{dc} is the diffusion–chemisorption rate constant. The plot of ($t^{1/2}/q_t$) versus $t^{1/2}$ yielded a straight line with a coefficient of correlation of R^2 = 0.9976, as shown in Figure S9 and Table 5.

The curve fits well with the diffusion–chemisorption model because the greater coefficient of correlation value (R^2 = 0.9981) is closer to 1 than the intraparticle diffusion model (R^2 = 0.5405). In addition, the calculated q_e (0.9158 $mg{\cdot}g^{-1}$) obtained by the slope of the diffusion–chemisorption equation was closer to the experimental q_e (1.03 $mg{\cdot}g^{-1}$). Hence, the adsorption of the drug could be well described by the diffusion–chemisorption model.

The intraparticle model plot shows that the intraparticle diffusion had a limited impact on the solute adsorption behaviour portrayed by the material and was not typical of the behaviour mostly portrayed by porous materials [34]. The high parameter value showed that the effect of the boundary layer was also responsible for the adsorption of CFX on the material. This meant that CFX adsorption was also influenced by the material's high surface area and functional groups [38,41]. Therefore, the adsorption rate of CFX to the material was determined by liquid film diffusion and surface adsorption [39,43].

4 Discussion

Sawdust is a multicomponent structural material composed of several aromatic polymers of lignin, carbohydrates, and non-structural components called extractives. The aromatic polymer of the lignin group comprises compounds such as *p*-coumaric acid, ferulic acid, caffeic acid, sinapic acid, vanillin, syringaldehyde, and vanillic acid. The carbohydrate fraction is mainly composed of hemicellulose and cellulose [44]. The extractives are a complex myriad of fats, waxes, proteins, terpenes, gums, resins, simple sugars, starches, phenolics, essential oils, pectins, mucilages, glycosides, saponins, fatty acids, sterols, and flavonoids [45]. Therefore, the diverse functional groups identified in the treated and untreated material originate from all the mentioned compounds. However, the reactions in this study targeted cellulose, as it is known to react with CA to introduce acidic functional groups in the material. However, the presence of other substances might interfere with this reaction. The materials were chemically and morphologically characterized using various techniques, followed by adsorption and kinetic studies.

4.1 Material characterization

The first characterization tool was FTIR, which evaluated the functional group composition of the materials after the reactions. The functional group composition changed when the sawdust was subjected to various treatments

(water, NaOH, and CA). When the material was treated with CA, the free primary alcohol groups in the cellulose reacted with some carboxyl groups in the CA (Figure S1). This explains the variations in the amount of OH groups when different amounts of CA were used (Table S1, Figure 1). This signalled a successful reaction between the CA and cellulose. The interaction of the sawdust with water and NaOH also brought changes that could be due to the saponification of esters associated with methylated carboxyl, which increases the number of free carboxylate groups. NaOH treatment also releases free primary alcohol groups esterified in cellulose molecules. The water and NaOH also remove low-molecular-weight soluble substances called extractives [46,47]. These phenomena may explain the increases in the peaks associated with the OH functionality in the FTIR data (Figure 1 and Table S1). The hydroxyl groups in cellulose could also combine with CA anhydride to form some ester linkages (peaks at 2,898–2,901 cm^{-1} assigned to the C–H group; peaks around 1,716–1,718 and 1,641–1,648 cm^{-1} assigned to the C═O group in ester, carboxylic acid, and aromatic lignin). Compared with the IR spectrum of the USC material samples, it could be seen that there was a strong characteristic stretching vibration absorption band of carboxyl groups around 1,716–1,718 cm^{-1} in the IR spectrum of CATSC samples, and this reflected the CA and esters. Furthermore, the broad absorption peaks around 3,342–3,345 cm^{-1} also confirmed the presence of more carboxylic O–H groups (Table S1). Therefore, the FTIR results (Figure 1, Table S1) showed that CA treatment significantly impacted the surface chemistry, which is relevant to the mechanism of interaction with CFX (Section 4.4).

Then, PZC was conducted using the salt addition method and found to be 2.3 (Figure 2). The results meant that the adsorbent's surface was negatively charged above pH 2.3 and positively charged below it [48]. The salt addition method has been primarily used to determine the PZC of natural organic substrates or vegetable wastes. Obtaining statistical agreement between PZC data from different authors is unclear because it mostly depends on substrate origin and the method used [24].

To evaluate the crystalline and amorphous nature of the materials, XRD was conducted and the results are presented in Figure 3 and Table 1. The structure of natural cellulosic fibres has crystalline and amorphous regions. A comparison of the XRD data shows that the USC and CATSC materials had no significant differences in their crystallinity indexes. This shows that the degree of crystallinity was not affected by the treatment or differences in CA concentrations. But, the results showed that the USC and CATSC crystalline and amorphous parameters differed randomly with concentration changes. However, the results of microscopic evaluation using STEM and SEM techniques showed that the USC and CATSC materials had significant differences in elemental composition, particle sizes, and distances (Figure 4; Tables 2–4). All the SEM images showed that the materials had irregularly distributed pores of varying sizes and some breakage of the cellulose, lignin, and hemicellulose structures. The apparent observation in the STEM images showed that both the amorphous and crystalline particle sizes and distributions are similar for all the materials. Although there are differences in the breakage patterns for the different materials, there is no clear relationship to the changes in the concentration of CA. This is also observed in the image analysis results, with evidence of changes in particle size and distance but no linear relationship with the CA concentration (Tables 3 and 4), suggesting that the backbone of the material remained intact despite the various acid treatments. Therefore, to have significant changes to the material, other treatments are needed to break the underlying bonds for maximum interaction of the CA with the material and produce a material that might have more improved properties than those exhibited in this study. However, the SEM EDX results showed a significant change in the C and O content for 0.14 M CATSC material. This could be attributed to the amount of CA reacting with the sawdust cellulose compared to the other concentrations. These changes might have contributed to the modification in the material's surface charges that led to the enhanced removal efficiency of CFX. The results obtained here are 56.76% for C and 43.23% for O, which is comparable and within the ranges reported in the literature for acid-treated cellulose materials. Reported values are in the range of 27–58% for C and 0.03–72.50% for O [21].

4.2 Adsorption studies

The results indicated that CATSC materials had higher removal efficiencies than USC materials. This can be attributed to the increased number of functional groups, particularly carboxyl groups (Figure 1). According to Figure 1 and Table S1 results, both CATSC and USC materials had an increased number of OH functional groups, yet only CATSC materials had increased removal efficiency. This could be attributed to the ionizable functional groups brought by CA that provide electrostatic interactions, additional and stronger hydrogen-bonding interactions, as well as increased surface area for interactions (Figure 1, Table S1). Base treatment and carboxylic acid functional group addition to cellulose by CA treatment are known to enhance cation-exchange

capability significantly in materials [46]. On the other hand, the lower activity in USC material could be due to the hindrance of lignin, hemicellulose molecules, and extractives.

The activity showed an irregular removal efficiency trend among the CATSC materials as the CA concentration increased, as shown in Figures 5 and 6. This could be attributed to the formation of crosslinking chain reactions and hydrogen bonds among the introduced CA residues on the cellulose surface (Figure S1), depending on the concentration that would mask the responsible functional groups for the CFX removal activity [23,49]. According to Nasution et al., CA can act as a crosslinking agent for methylcellulose molecules, producing a crosslinked molecule like hydrogels, which then decrease water vapour permeability, swelling, and increased gas barrier properties (decreased pores, decreased water, and oxygen affinity), and this could occur at lower concentrations like 5% CA w/w [50]. A similar study on the synthesis of CA-based carboxymethyl starch-based films showed that increased CA concentration also increased crosslinking [51]. Another study also showed that methylcellulose produced a hydrogel with increasing equilibrium swelling/average swelling values as the CA % increased from 5% to 3%, whereas 1% had no significant difference from the control [52]. In this study, crosslinking in the synthesized materials was also observed in the FTIR spectrum peak at 1,716–1,718 $cm^{-1,}$ which increased to the highest level in CATSC treated with 1.12 M CA (Table S1, Figure 1). Statistical results also showed that the CA treatment had an impact on surface chemistry, with functional groups at 3,835–3,840 cm^{-1} (R^2 = 0.9026, p = 0.0054 and <0.05) and 2,160–2,163 cm^{-1} (R^2 = 0.8033, p = 0.0296 and <0.05) having a significant impact on the removal efficiency of the materials.

4.3 Factors that affect the removal of CFX

Various factors known to affect adsorption efficiency and capacity, such as CFX loading dose, time, adsorbate mass, pH, and temperature, were investigated as reported in similar studies [48,53,54]. The data on the impact of the loading dose on the removal of CFX showed a sudden decrease from 100% to 55% at the 5 ppm loading dose for the 0.14 M CA material, followed by a gradual increase and stabilization around 70% above the 12 ppm CFX loading. It may be due to mass transfer resistance to CFX adsorption at the interface between the solid and aqueous phases and the fact that higher initial CFX concentrations above 12 ppm provide a driving force to overcome the resistance. The results are similar to a study by Wakejo et al., whereby increasing the CFX initial concentration from 10 to 40 $mg{\cdot}L^{-1}$ decreased the CFX removal efficiency from 100 to 76% at pH (7.5), adsorbent dose (0.5 $g{\cdot}L^{-1}$), and contact time (46.25 min). However, the CFX adsorption capacity increased from 20 to 60 $mg{\cdot}g^{-1}$ when the initial CFX concentration changed from 10 to 40 $mg{\cdot}L^{-1}$. They also attributed it to the reduction of the resistance to CFX uptake from the aqueous solution [39]. Similarly, a study by Yousefi et al., where CFX concentration was increased from 30 to 100 $mg{\cdot}L^{-1}$, showed a decrease in CFX removal efficiency from 83% to 59% [55]. However, in the study by Wang et al., the adsorption capacity of cationic CFX increased very quickly for CFX initial concentrations of less than 50 $mg{\cdot}L^{-1}$ but decreased as the CFX initial concentration was increased beyond 50 $mg{\cdot}L^{-1}$ [56]. This was attributed to the lack of available sites on the adsorbent for the uptake of excess CFX at higher concentrations [57]. The observed trend of adsorption capacity increases with an increase in the loading dose of CFX beyond a certain concentration, may be attributed to the improved adsorbate–adsorbent interaction at the adsorbent binding sites. However, a further increase in the loading dose leads to binding site saturation, whereby the adsorption capacity remains constant irrespective of CFX concentration [41]. Similar results were observed in several reported studies, including those by Gulen and Demircivi, where a 2:1 dioctahedral clay structure increased CFX adsorption from 1.8% (0.034 $g{\cdot}L^{-1}$) to 99.2% (2 $g{\cdot}L^{-1}$) [58]; and those by Shang et al., where the CFX removal efficiency increased from 36% to 100% for a herbal residue biochar when the dosage increased from 0.025 to 0.5 $g{\cdot}L^{-1}$ [59].

The results also showed that the extent of CFX removal (%) increased with increasing solution pH until the maximum removal occurred in the pH range of 4.5–5 (Figure 7c). The removal efficiency decreased slightly to pH 6, after which the efficiency increased slowly. This removal efficiency behaviour is attributed to the surface charge of the adsorbents and the state of the CFX across the different pH ranges (Figures 2 and 7d). The substrate's performance depends on many factors, such as surface functional groups, the presence or absence of anions and cations, and the availability and size of the porous structure in the precursors [30]. Most natural and organic substrates possess functional groups such as carboxyl, sulfhydryl, hydroxyl, and amino groups that give rise to negative or positive charges on their surface upon ionization. The magnitude of the surface charge depends on the type of function and the pH of the solution and material PZC [24]. The PZC is a pH value at which the net charge of the surface components equals zero (same amounts of positive and negative charges) at a specific temperature, applied pressure, and aqueous solution composition. PZC values help optimize substrate selection

for adsorption. Substrates with low PZC values are suitable for cations, while those with high PZC values are suitable for anions (Figures 2 and 7d).

The results presented in this study are similar to those reported by Wakejo et al., where the CFX removal efficiency of a modified bamboo char material increased with an increase in pH (5.25–7.5) followed by a decrease, and by Dehghan et al., where CFX removal efficiency using a metal–organic framework increased with an increase in pH (3–7.5) followed by a decrease. All the decreases in efficiency were in the zwitterion stage of the CFX molecule. The adsorption behaviour was attributed to protonation–deprotonation reactions between the CFX molecules and the materials [39,60].

Reaction time was also a factor that was investigated for effects on adsorption, and the results showed that removal efficiency increased with time at a decreasing rate until it became constant (Figure 7e). This may be attributed to the availability of abundant free active sites of the material in the early stages of the process, followed by saturation of the active sites over time. The stage at which no significant change was observed was chosen as the equilibrium time, and it was used for all the experiments. Similar results were also reported in the literature [39,57]. On the other hand, temperature increases affect removal efficiency (Figure 7f). This meant an increment in temperature affected the uptake of CFX, which was also confirmed by the negative value of delta H calculated for the thermodynamic isotherms (Table 5).

4.4 Possible mechanisms for CFX adsorption

Based on the adsorption mechanism described by Tatarchuk et al., the key mechanistic pathway of adsorption of CFX to the CATSC material is postulated to be chemisorption [61]. A simplified diagram highlighting CATSC interactions with the zwitterionic form of CFX is illustrated schematically in Figure 7d. Chemisorption occurs when adsorbent and adsorbate have complementary functional groups such as amine ($-NH_2$), carboxylic acid (−COOH), and hydroxyl (−OH). The CATSC material and CFX satisfy this condition and are bound via H-bonding and electrostatic attraction. This is evidenced by the improved adsorption efficiency of the treated CATSC materials when compared to the parent material (USC). Adsorption by chemisorption also involves charge transfer, exchange, or sharing of electrons. In this case, there were changes in the state of the material charges (COOH to COO^- after PZC) and the CFX with changes in solution pH (anionic, zwitterionic, and cationic) due to the charge transfer processes (Figure 7d). This is because variation in solution pH affects the availability of ionizable functional groups in the CATSC and CFX, leading to enhanced electrostatic interactions, additional and stronger hydrogen-bonding interactions, and an increased surface area for interactions (Figure 1, Table S1). The piperazine rings in the CFX molecules are positively charged (NH_2^+) in the neutral phase of the solution. They created an attraction between CFX^+ and the negatively charged surface of the material, releasing additional H^+ in the process [62]. Additionally, the C–H and C═C groups in the aromatic rings of the remaining lignin molecules also interact with the CFX via π–π interactions (Figures 1 and 7d; Table S1). In summary, π–π donor–acceptor interactions, electrostatic attractions, and H-bonding interactions are responsible for CFX adsorption. The proposed mechanism is supported by the kinetic model; the pseudo-second-order model has shown that the adsorption of CFX is favoured and controlled by the chemisorption process. Also, the Temkin model showed that the adsorption process follows the chemisorption process. Similarly, chemisorption is characterised by exothermic reactions, and the thermodynamic model showed that the adsorption process was exothermic.

5 Conclusions

The adsorption of CFX dissolved in water was achieved at up to 20 $mg{\cdot}L^{-1}$ concentration with over 70% efficiency and 100% removal at 1 $mg{\cdot}L^{-1}$ within 40 min of contact. This is important because the long-term environmental impact of CFX and other large-volume antibiotics in water, even at very low concentrations, is still not fully understood. The CATSC is a very effective adsorbent for CFX that is below its saturation levels. The adsorption process was interpreted in terms of the Langmuir, Freundlich, and Temkin isotherm models, with the latter agreeing well with the adsorption parameters and data range. Overall, the CA-treated sawdust material showed potential for the adsorption of CFX for a wide variety of applications that may include drug removal from aqueous environments, gut decontamination (in case of an overdose or poisoning), drug delivery, including wound dressing, and solid support for phase extraction, with further studies needed to optimize the conditions and material properties for each potential application. Despite some of the limitations highlighted in this study, there is enormous potential for using inexpensive, readily available, and sustainably produced sawdust and CA-based materials for the mentioned adsorption applications of CFX and related quinolone antibiotics in aqueous environments.

Acknowledgement: The authors thank UKZN and the National Research Foundation of South Africa for their financial support. IC also thanks Kamuzu University of Health Sciences Malawi for a paid study leave. The authors also thank Prof. Marya Lieberman of the University of Notre Dame, USA, for supplying the reference standards.

Funding information: This research was funded by University of KwaZulu-Natal (UKZN) and the National Research Foundation (NRF) of South Africa.

Author contributions: Ibrahim Chikowe: conceptualization; writing – original draft, methodology, investigation; and formal analysis. Muhammad Dabai Bala: conceptualization; funding acquisition; supervision; writing – review and editing; and project administration.

Conflict of interest: Authors state no conflict of interest.

Data availability statement: The datasets generated during and/or analysed during the current study are available from the corresponding author on reasonable request.

References

[1] Ebrahimi R, Salavaty M. Controlled drug delivery of ciprofloxacin from ultrasonic hydrogel. E-Polymers. 2018;18:187–95. doi: 10.1515/epoly-2017-0123.

[2] Sophia AC, Lima EC. Removal of emerging contaminants from the environment by adsorption. Ecotoxicol Env Saf. 2018;150:1–17. doi: 10.1016/j.ecoenv.2017.12.026.

[3] Zellner T, Prasa D, Färber E, Hoffmann-Walbeck P, Genser D, Eyer F. The use of activated charcoal to treat intoxications. Dtsch Arztebl Int. 2019;116:311–7. doi: 10.3238/arztebl.2019.0311.

[4] Eboka CJ, Afolabi AB. In-vitro adsorption of fluoroquinolones on some pharmaceutical adsorbents. Tropical J Pharm Res. 2007;5:533–8. doi: 10.4314/tjpr.v5i1.14629.

[5] Xiao J, Wang J, Fan H, Zhou Q, Liu X. Recent advances of adsorbents in solid phase extraction for environmental samples. Int J Env Anal Chem. 2016;96:407–35. doi: 10.1080/03067319.2016.1150459.

[6] Ma J, Xiong Y, Dai X, Yu F. Coadsorption behavior and mechanism of ciprofloxacin and Cu(II) on graphene hydrogel wetted surface. Chem Eng J. 2020;380:122387. doi: 10.1016/j.cej.2019.122387.

[7] Aragaw TA, Bogale FM. Biomass-based adsorbents for removal of dyes from wastewater: a review. Front Env Sci. 2021;9:1–24. doi: 10.3389/fenvs.2021.764958.

[8] Ferreira VRA, Amorim CL, Cravo SM, Tiritan ME, Castro PML, Afonso CMM. Fluoroquinolones biosorption onto microbial biomass: Activated sludge and aerobic granular sludge. Int Biodeterior Biodegrad. 2016;110:53–60. doi: 10.1016/j.ibiod.2016.02.014.

[9] Girardi C, Greve J, Lamshöft M, Fetzer I, Miltner A, Schäffer A, et al. Biodegradation of ciprofloxacin in water and soil and its effects on the microbial communities. J Hazard Mater. 2011;198:22–30. doi: 10.1016/j.jhazmat.2011.10.004.

[10] Aldossary HA, Khalaf MM, Gouda M, Elmushyakhi A, Abou Taleb MF, Abd El-Lateef HM. Wound dressing candidate materials based on casted films of cellulose acetate modified with zirconium oxide (ZrO_2), and gallium oxide (Ga_2O_3). Mater Today Commun. 2023;34:105299. doi: 10.1016/j.mtcomm.2022.105299.

[11] Huang L, Wang M, Shi C, Huang J, Zhang B. Adsorption of tetracycline and ciprofloxacin on activated carbon prepared from lignin with H_3PO_4 activation. Desalin Water Treat. 2014;52:2678–87. doi: 10.1080/19443994.2013.833873.

[12] Genç N, Dogan EC. Adsorption kinetics of the antibiotic ciprofloxacin on bentonite, activated carbon, zeolite, and pumice. Desalin Water Treat. 2015;53:785–93. doi: 10.1080/19443994.2013.842504.

[13] Wang CJ, Li Z, Jiang WT. Adsorption of ciprofloxacin on 2:1 dioctahedral clay minerals. Appl Clay Sci. 2011;53:723–8. doi: 10.1016/j.clay.2011.06.014.

[14] Li Z, Hong H, Liao L, Ackley CJ, Schulz LA, MacDonald RA, et al. A mechanistic study of ciprofloxacin removal by kaolinite. Colloids Surf B Biointerfaces. 2011;88:10895–904. doi: 10.1016/j.colsurfb.2011.07.011.

[15] Zhang H, Huang CH. Adsorption and oxidation of fluoroquinolone antibacterial agents and structurally related amines with goethite. Chemosphere. 2007;66:1502–12. doi: 10.1016/j.chemosphere.2006.08.024.

[16] Rakshit S, Sarkar D, Elzinga EJ, Punamiya P, Datta R. Mechanisms of ciprofloxacin removal by nano-sized magnetite. J Hazard Mater. 2013;246–247:221–6. doi: 10.1016/j.jhazmat.2012.12.032.

[17] Jiang WT, Chang PH, Wang YS, Tsai Y, Jean JS, Li Z, et al. Removal of ciprofloxacin from water by birnessite. J Hazard Mater. 2013;250–251:362–9. doi: 10.1016/j.jhazmat.2013.02.015.

[18] Dubey U, Maurya A, Rawat M, Tiwari D, Chalotra A. Synthesis of adsorbent from rubberwood sawdust (Hevea brasiliensis). Mater Today Proc. 2023. doi: 10.1016/j.matpr.2023.01.345.

[19] Gupta VK, Carrott PJM, Ribeiro MML, Suhas C. Critical reviews in environmental science and technology low-cost adsorbents: Growing approach to wastewater treatment-a review. Vol. 39. London, UK: Taylor & Francis; 2009. p. 783–842.

[20] Pimentel CH, Freire MS, Gómez-Díaz D, González-Álvarez J. Preparation of activated carbon from pine (Pinus radiata) sawdust by chemical activation with zinc chloride for wood dye adsorption. Biomass Convers Biorefin. 2023;16537–55. doi: 10.1007/s13399-023-04138-4.

[21] Adegoke KA, Adesina OO, Okon-Akan OA, Adegoke OR, Olabintan AB, Ajala OA, et al. Sawdust-biomass based materials for sequestration of organic and inorganic pollutants and potential for engineering applications. Curr Res Green SustaChem. 2022;5:100274–312. doi: 10.1016/j.crgsc.2022.100274.

[22] Singh SK, Kaldate R, Bisht A. Citric acid, antioxidant effects in health. Antioxid Eff Health: Bright Dark Side. 2022;309–22. doi: 10.1016/B978-0-12-819096-8.00045-8.

[23] Meftahi A, Khajavi R, Rashidi A, Rahimi MK, Bahador A. Preventing the collapse of 3D bacterial cellulose network via citric acid. J Nanostruct Chem. 2018;8:311–20. doi: 10.1007/s40097-018-0275-4.

[24] Bakatula EN, Richard D, Neculita CM, Zagury GJ. Determination of point of zero charge of natural organic materials. Environ Sci Pollut Res. 2018;25:7823–33. doi: 10.1007/s11356-017-1115-7.

[25] Al-Maliky EA, Gzar HA, Al-Azawy MG. Determination of point of zero charge (PZC) of concrete particles adsorbents. IOP Conf Ser Mater Sci Eng. 2021;1184:012004. doi: 10.1088/1757-899x/1184/1/012004.

[26] Movasaghi Z, Yan B, Niu C. Adsorption of ciprofloxacin from water by pretreated oat hulls: Equilibrium, kinetic, and thermodynamic studies. Ind Crop Prod. 2019;127:237–50. doi: 10.1016/j.indcrop.2018.10.051.
[27] Patel M, Kumar R, Pittman CU, Mohan D. Ciprofloxacin and acetaminophen sorption onto banana peel biochars: Environmental and process parameter influences. Env Res. 2021;201:111218. doi: 10.1016/j.envres.2021.111218.
[28] Park S, Baker JO, Himmel ME, Parilla PA, Johnson DK. Cellulose crystallinity index: Measurement techniques and their impact on interpreting cellulase performance. Biotechnol Biofuels. 2010;3:1–10. doi: 10.1186/1754-6834-3-10.
[29] Najafpoor AA, Nemati Sani O, Alidadi H, Yazdani M, Navaei Fezabady AA, Taghavi M. Optimization of ciprofloxacin adsorption from synthetic wastewaters using γ-Al_2O_3 nanoparticles: An experimental design based on response surface methodology. Colloids Interface Sci Commun. 2019;33:100212–8. doi: 10.1016/j.colcom.2019.100212.
[30] Sun Y, Li H, Li G, Gao B, Yue Q, Li X. Characterization and ciprofloxacin adsorption properties of activated carbons prepared from biomass wastes by H_3PO_4 activation. Bioresour Technol. 2016;217:239–44. doi: 10.1016/j.biortech.2016.03.047.
[31] Barrett LM. Wastewater treatment: Processes, management strategies and environmental/health impacts. Hauppauge, New York: Nova Science Publishers, Inc.; 2015.
[32] Liang R, Hu A, Hatat-Fraile M, Zhou N. Fundamentals on adsorption, membrane filtration, and advanced oxidation processes for water treatment. Nanotechnol Water Treat Purif. 2014;1–45. doi: 10.1007/978-3-319-06578-6_1.
[33] Balarak D, Mahvi AH, Shim MJ, Lee SM. Adsorption of ciprofloxacin from aqueous solution onto synthesized NiO: Isotherm, kinetic and thermodynamic studies. Desalin Water Treat. 2021;212:390–400. doi: 10.5004/dwt.2021.26603.
[34] Ngeno EC, Orata F, Baraza LD, Shikuku VO, Kimosop SJ. Adsorption of caffeine and ciprofloxacin onto pyrolitically derived water hyacinth biochar: isothermal, kinetic and thermodynamic studies. J Chem Chem Eng. 2016;10:185–94. doi: 10.17265/1934-7375/2016.04.006.
[35] Langmuir I. The adsorption of gases on plane surfaces of glass, mica and platinum. J Am Chem Soc. 1918;40:1361–403. doi: 10.1021/ja02242a004.
[36] Azmi SNH, Al Lawati WM, Al Hoqani UHA, Al Aufi E, Al Hatmi K, Al Zadjali JS, et al. Development of a citric-acid-modified cellulose adsorbent derived from Moringa peregrina leaf for adsorptive removal of citalopram HBr in aqueous solutions. Pharmaceuticals. 2022;15:760–78. doi: 10.3390/ph15060760.
[37] Stylianou M, Christou A, Michael C, Agapiou A, Papanastasiou P, Fatta-Kassinos D. Adsorption and removal of seven antibiotic compounds present in water with the use of biochar derived from the pyrolysis of organic waste feedstocks. J Env Chem Eng. 2021;9:105868. doi: 10.1016/j.jece.2021.105868.
[38] Kiurski J, Adamović S, Oros I, Krstić J, Kovačević I. Adsorption feasibility in the Cr(total) ions removal from waste printing developer. Glob Nest J. 2012;14:18–23. doi: 10.30955/gnj.000810.
[39] Wakejo WK, Meshasha BT, Kang JW, Chebude Y. Enhanced ciprofloxacin removal from aqueous solution using a chemically modified biochar derived from bamboo sawdust: adsorption process optimization with response surface methodology. Adsorpt Sci Technol. 2022;2022:1–23. doi: 10.1155/2022/2699530.
[40] Togue Kamga F. Modeling adsorption mechanism of paraquat onto Ayous (Triplochiton scleroxylon) wood sawdust. Appl Water Sci. 2019;9:1–7. doi: 10.1007/s13201-018-0879-3.
[41] Atugoda T, Gunawardane C, Ahmad M, Vithanage M. Mechanistic interaction of ciprofloxacin on zeolite modified seaweed (Sargassum crassifolium) derived biochar: Kinetics, isotherm and thermodynamics. Chemosphere. 2021;281:130676. doi: 10.1016/j.chemosphere.2021.130676.
[42] Kooh MRR, Dahri MK, Lim LBL. Removal of methyl violet 2B dye from aqueous solution using Nepenthes rafflesiana pitcher and leaves. Appl Water Sci. 2017;7:3859–68. doi: 10.1007/s13201-017-0537-1.
[43] Huang W, Chen J, Zhang J. Removal of ciprofloxacin from aqueous solution by rabbit manure biochar. Environ Technol (U Kingd). 2020;41:1380–90. doi: 10.1080/09593330.2018.1535628.
[44] Sudarsanam P, Ruijten D, Liao Y, Renders T, Koelewijn SF, Sels BF. Towards lignin-derived chemicals using atom-efficient catalytic routes. Trends Chem. 2020;2:898–913. doi: 10.1016/j.trechm.2020.07.011.
[45] Pattiya A. Fast pyrolysis. Direct thermochemical liquefaction for energy applications. 2018;3–28. doi: 10.1016/B978-0-08-101029-7.00001-1.
[46] Thanh ND, Nhung HL. Cellulose modified with citric acid and its absorption of Pb^{2+} and Cd^{2+} ions. Proceedings of the 13th International Electronic Conference on Synthetic Organic Chemistry, 1–30 November 2009, MDPI: Basel, Switzerland. doi: 10.20372/eajs.v13i2.801.
[47] Mohamad Zaidi NAH, Sallehuddin FN, Lim LBL, Kooh MRR. Surface modification of Artocarpus odoratissimus leaves using NaOH, SDS and EDTA to enhance adsorption of toxic crystal violet dye. Int J Env Anal Chem. 2023;103:1836–54. doi: 10.1080/03067319.2021.1884238.
[48] Suhaimi N, Kooh MRR, Lim CM, Chou Chao CT, Chou Chau YF, Mahadi AH, et al. The use of gigantochloa bamboo-derived biochar for the removal of methylene blue from aqueous solution. Adsorpt Sci Technol. 2022;2022:1–12. doi: 10.1155/2022/8245797.
[49] Salihu R, Abd Razak SI, Ahmad Zawawi N, Rafiq Abdul Kadir M, Izzah Ismail N, Jusoh N, et al. Citric acid: A green cross-linker of biomaterials for biomedical applications. Eur Polym J. 2021;146:110271–82. doi: 10.1016/j.eurpolymj.2021.110271.
[50] Nasution H, Harahap H, Dalimunthe NF, Ginting MHS, Jaafar M, Tan OOH, et al. Hydrogel and effects of crosslinking agent on cellulose-based hydrogels: A review. Gels. 2022;8:568–98. doi: 10.3390/gels8090568.
[51] Wilpiszewska K, Antosik AK, Zdanowicz M. The effect of citric acid on physicochemical properties of hydrophilic carboxymethyl starch-based films. J Polym Env. 2019;27:1379–87. doi: 10.1007/s10924-019-01436-9.
[52] Bonetti L, De Nardo L, Farè S. Chemically crosslinked methylcellulose substrates for cell sheet engineering. Gels. 2021;7:141–54. doi: 10.3390/gels7030141.
[53] Xu Y, Gu Y, Peng L, Wang N, Chen S, Liang C, et al. Unravelling ciprofloxacin removal in a nitrifying moving bed biofilm reactor: Biodegradation mechanisms and pathways. Chemosphere. 2023;320:138099. doi: 10.1016/j.chemosphere.2023.138099.
[54] Mirizadeh S, Solisio C, Converti A, Casazza AA. Efficient removal of tetracycline, ciprofloxacin, and amoxicillin by novel magnetic chitosan/microalgae biocomposites. Sep Purif Technol. 2024;329:125115–27. doi: 10.1016/j.seppur.2023.125115.

[55] Yousefi M, Gholami M, Oskoei V, Mohammadi AA, Baziar M, Esrafili A. Comparison of LSSVM and RSM in simulating the removal of ciprofloxacin from aqueous solutions using magnetization of functionalized multi-walled carbon nanotubes: Process optimization using GA and RSM techniques. J Env Chem Eng. 2021;9:105677. doi: 10.1016/j.jece.2021.105677.

[56] Wang YX, Gupta K, Li JR, Yuan B, Yang JCE, Fu ML. Novel chalcogenide based magnetic adsorbent KMS-1/L-Cystein/Fe3O4 for the facile removal of ciprofloxacin from aqueous solution. Colloids Surf A Physicochem Eng Asp. 2018;538:378–86. doi: 10.1016/j.colsurfa.2017.11.016.

[57] El-Bendary N, El-Etriby HK, Mahanna H. Reuse of adsorption residuals for enhancing removal of ciprofloxacin from wastewater. Environ Technol (U Kingd). 2022;43:4438–54. doi: 10.1080/09593330.2021.1952310.

[58] Gulen B, Demircivi P. Adsorption properties of flouroquinolone type antibiotic ciprofloxacin into 2:1 dioctahedral clay structure: Box-Behnken experimental design. J Mol Struct. 2020;1206:127659. doi: 10.1016/j.molstruc.2019.127659.

[59] Shang JG, Kong XR, He LL, Li WH, Liao QJH. Low-cost biochar derived from herbal residue: characterization and application for ciprofloxacin adsorption. Int J Environ Sci Technol. 2016;13:2449–58. doi: 10.1007/s13762-016-1075-3.

[60] Dehghan A, Mohammadi AA, Yousefi M, Najafpoor AA, Shams M, Rezania S. Enhanced kinetic removal of ciprofloxacin onto metal-organic frameworks by sonication, process optimization and metal leaching study. Nanomaterials. 2019;9:1422–38. doi: 10.3390/nano9101422.

[61] Tatarchuk T, Soltys L, Macyk W. Magnetic adsorbents for removal of pharmaceuticals: A review of adsorption properties. J Mol Liq. 2023;384:122174–95. doi: 10.1016/j.molliq.2023.122174.

[62] Li J, Yu G, Pan L, Li C, You F, Wang Y. Ciprofloxacin adsorption by biochar derived from co-pyrolysis of sewage sludge and bamboo waste. Environ Sci Pollut Res. 2020;27:22806–17. doi: 10.1007/s11356-020-08333-y.